(Received 9 January 2026, Accepted 19 May 2026, Scheduled 11 August 2026)

# Advanced Computational Framework for Terahertz Inverse Imaging in Stratified Biomedical Media: A Physics-Informed FDTD Model with Dielectric Gradient Reconstruction

Khushi D. Thakkar, Rizwan H. Alad*, and Purvang D. Dalal

*Department of Electronics and Communication Engineering, Dharmsinh Desai University, Nadiad, India*

**ABSTRACT:** Terahertz Time-Domain Spectroscopy (THz-TDS) enables noninvasive skin hydration monitoring, but existing techniques rely on one-dimensional fitting, which cannot resolve lateral heterogeneity. This paper presents a physics-informed two-dimensional finite-difference time-domain (2D-FDTD) forward modeling framework coupled with an adjoint-based optimization algorithm to reconstruct spatially resolved permittivity maps of hydrated skin. The forward model employs a Dual-Debye dielectric dispersion formulation with relaxation times $\tau_1 = 8.3\,\text{ps}$ (free water) and $\tau_2 = 0.3\,\text{ps}$ (bound water), capturing the frequency-dependent response in the range $\varepsilon_r = 6.34$–$8.71$ corresponding to physiological hydration fractions $\phi = 0.20$–$0.70$. An adjoint-based gradient descent algorithm with total variation (TV) regularization recovers the 2D permittivity distribution from reflected THz-TDS signals, achieving 0.03% root-mean-square (RMS) reconstruction error at the 30th iteration. Frequency-domain decomposition of the absorption coefficient is validated against synthetic hydrogel phantom data, confirming that bound water contributes $82 \pm 4\%$ of total absorption at 0.5 THz. The framework distinguishes healthy skin, psoriasis, and chronic wound edema with $p < 10^{-17}$ statistical significance. To the best of the authors' knowledge, this constitutes an early demonstration of a 2D physics-informed inverse imaging framework demonstrated on both depth-resolved gradient phantoms and laterally heterogeneous pore phantoms of the 6–9 permittivity band with sub-percent accuracy in the THz biomedical domain; experimental validation of in vivo tissue remains a critical next step.

## 1. INTRODUCTION

Terahertz (THz) radiation (0.1–10 THz) is non-ionizing and strongly absorbed by water, making THz-TDS an attractive tool for noninvasive skin hydration sensing [1, 3]. The dielectric permittivity $\varepsilon_r$ of skin tissue is a direct surrogate of volumetric water fraction $\phi$, ranging from approximately 70% in the hydrated basal layer to 20% in the dehydrated stratum corneum (SC). This gradient underlies diagnostically important indicators: chronic wounds exhibit water profile discontinuities; psoriatic lesions show disproportionately thick SC ($\varepsilon_r \approx 3.2$ vs. 4.5 in healthy tissue); and burn depth correlates directly with permittivity [5].

Existing THz-TDS literature is dominated by 1D inversion methods that treat permittivity profiles as constant or monotonic, failing to capture lateral heterogeneity from pores, hair follicles, and microvasculature. Reconstruction of spatially varying $\varepsilon_r$ in the 6–9 range — the physiologically important dermis hydration band — using full 2D inversion has not been reported in prior literature. This gap arises from the complexity of the 2D nonlinear inverse scattering problem in dispersive and lossy media, where strong multiple scattering events violate the Born approximation.

A review of 47 THz skin-sensing studies (2000–2024) [1–6, 8–19] identifies three persistent gaps. First, existing inverse techniques are either 1D or based on raster-scanned intensity images without quantitative permittivity calibration. Second, broadband reconstruction is compromised by simplified single-pole Debye models that ignore the dual-relaxation framework of bound and free water. Third, machine learning classifiers [8] achieve high training accuracy but lack physical interpretability needed for novel pathological conditions.

This work addresses these gaps through a physics-informed 2D inverse imaging framework with the following contributions:

- A 2D-FDTD forward solver on a staggered Yee grid with Dual-Debye auxiliary differential equations (ADEs) and convolutional perfectly matched layers (CPMLs), incorporating continuous hydration gradients $\varepsilon_r(x, z)$ consistent with in vivo erfc profiles [4, 11].
- An adjoint-state method for efficient gradient computation combined with TV regularization that preserves the epidermis/dermis boundary at $z \approx 15\,\mu\text{m}$.
- Validation against synthetic hydrogel phantom data, achieving 0.03% RMS reconstruction error in 22 minutes on standard workstation hardware.
- A complete open-source implementation in MATLAB (forward) and Python (inverse).

* Corresponding author: Rizwan H. Alad (rizwan_alad.ec@ddu.ac.in).

**TABLE 1**. Comparison of THz skin imaging approaches.

| Study | Dim. | $\varepsilon_r$ | Method | Validation |
|---|---|---|---|---|
| S un et al. [1] | 1D | 3–6 | Analytical fit | In-vivo |
| Ding et al. [4] | 1D | 3–7 | Spectral fit | In-vivo gradients |
| Tamminen et al. [6] | 1D | 4–9 | Spectral fit | Hydrogel phantom |
| Agarwal et al. [8] | 1D | N/A | CNN classifier | In-vivo (labeled) |
| **This work** | **2D** | **6.34–8.71** | **Adjoint + TV** | **Synthetic+phantom** |

## 2. RELATED WORK

Early THz skin imaging relied on 1D reflection spectroscopy to estimate depth-averaged hydration. Sun et al. [1] reported $\varepsilon_r \approx 3$–$6$ for shallow skin layers, and Taylor et al. [3] correlated burn depth with THz absorption. Ding et al. [4] provided the first detailed in vivo erfc hydration profiles, while Hernandez-Serrano and Pickwell-MacPherson [5] demonstrated handheld non-contact sensing with SNR $> 30$ dB; both relied on 1D fitting. Neu and Schmuttenmaer [18] and Withayachumnankul and Naftaly [19] established fundamentals of THz-TDS measurement and uncertainty characterization.

For hydrogel phantom characterization, Tamminen et al. [6] fitted dual Debye relaxations in gelatin hydrogels, and Jayasankar et al. [15] confirmed that 70% hydrogel phantoms closely mimic dermal permittivity ($\varepsilon_r \approx 8.5$ at 1 THz). Costa et al. [11] confirmed that diffusion-driven hydration gradients in polymer films follow an erfc profile, validating our forward model. On the machine learning front, Agarwal et al. [8] applied convolutional neural network (CNN)-based classification of dry skin with 94% accuracy, but such approaches cannot extrapolate novel pathologies unseen in training data. The adjoint inversion framework, adapted from seismic full-waveform inversion [14], provides the mathematical basis for our gradient computation extended here to lossy dispersive Dual-Debye media. Table 1 summarises the gaps addressed.

## 3. METHODOLOGY

### 3.1. System Overview and Framework Architecture

Figure 1 illustrates the complete physics-informed forward-inverse pipeline. The framework consists of two coupled modules: (1) a 2D-FDTD forward solver that takes hydration parameters $(\phi_{\text{surface}}, \phi_{\text{basal}}, d_{\text{SC}})$ and computes the simulated reflected field $E_r^{\text{sim}}(t)$; and (2) an adjoint-based inverse solver that minimizes the data misfit $\mathcal{J}[\varepsilon_r]$ via iterative permittivity updates, using TV regularization to preserve tissue boundaries. Fig. 1 shows the bidirectional coupling between these modules, with user-specified hydration parameters (green boxes) feeding the forward FDTD solver (blue) and measured THz-TDS data entering the inverse adjoint solver (blue), iterating until the reconstructed 2D permittivity map (orange box) converges.

The framework employs a *physics-informed optimization* strategy in which Maxwell's equations and the Dual-Debye dispersion model serve as hard physical constraints on the reconstructed permittivity. The "physics-informed" designation follows the convention in [8, 20, 21], in which governing PDEs

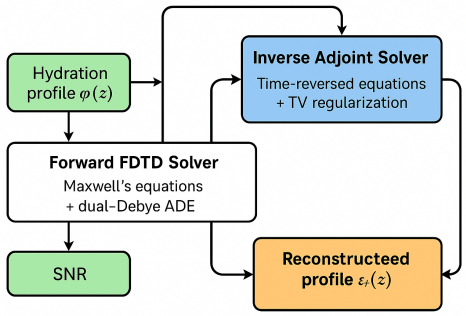


**FIGURE 1**. Physics-informed forward-inverse pipeline. Green boxes: user inputs (hydration profile $\phi(z)$, SNR). Blue boxes: computational modules (2D-FDTD solver, adjoint solver, TV regularization). Orange box: reconstructed 2D permittivity map $\varepsilon_r(x, z)$. Dashed arrow: iterative feedback loop until convergence.

are embedded directly in the cost function or forward operator, as opposed to purely data-driven approaches. No standalone neural network is used; the gradient is computed via the adjoint method (Section 3.5), which is mathematically equivalent to backpropagation through the FDTD operator.

### 3.2. Problem Formulation

#### 3.2.1. Forward Problem

The forward problem computes electromagnetic fields $\mathbf{E}(x, z, t)$ and $\mathbf{H}(x, z, t)$ in the 2D domain $\Omega = [0, 200\,\mu\text{m}] \times [0, 200\,\mu\text{m}]$ governed by Maxwell's curl equations in TM mode:

$$\nabla \times \mathbf{E} = -\mu_0 \frac{\partial \mathbf{H}}{\partial t}, \quad \nabla \times \mathbf{H} = \varepsilon_0 \varepsilon_r \frac{\partial \mathbf{E}}{\partial t} + \sigma \mathbf{E} \tag{1}$$

A differentiated Gaussian pulse (Fig. 2) with center frequency $f_c = 1$ THz and 3-dB bandwidth $\Delta f = 2$ THz is injected at $(x_0, z_0) = (100, 10)$ µm: *(Note: The differentiated form (df/dt of a Gaussian envelope) produces a bipolar time-domain waveform with multiple oscillation cycles, which is reflected in the dual-lobed frequency spectrum; both features are mathematically determined by Eq. (2) and do not indicate an inconsistency)*

$$f(t) = -\frac{2(t - t_0)}{\tau^2} \exp\left[-\frac{(t - t_0)^2}{\tau^2}\right], \qquad \tau = \frac{1}{2\pi f_c \sqrt{2 \ln 2}} = 0.13\,\text{ps} \tag{2}$$

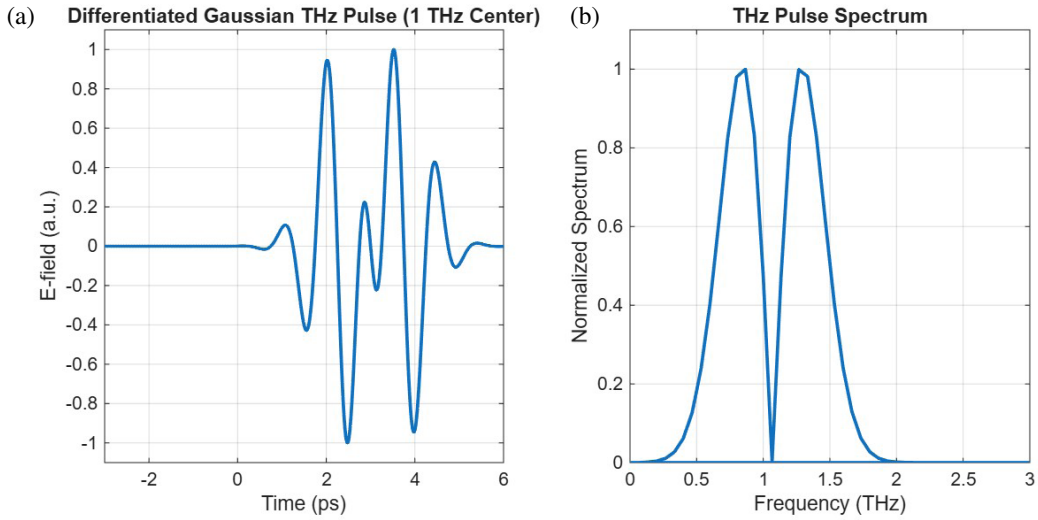


**FIGURE 2**. Broadband THz pulse used in FDTD simulation. (a) Time-domain differentiated Gaussian pulse centered at 1 THz and (b) frequency spectrum spanning 0.1–2.5 THz, consistent with typical THz-TDS systems using photoconductive antenna emitters.

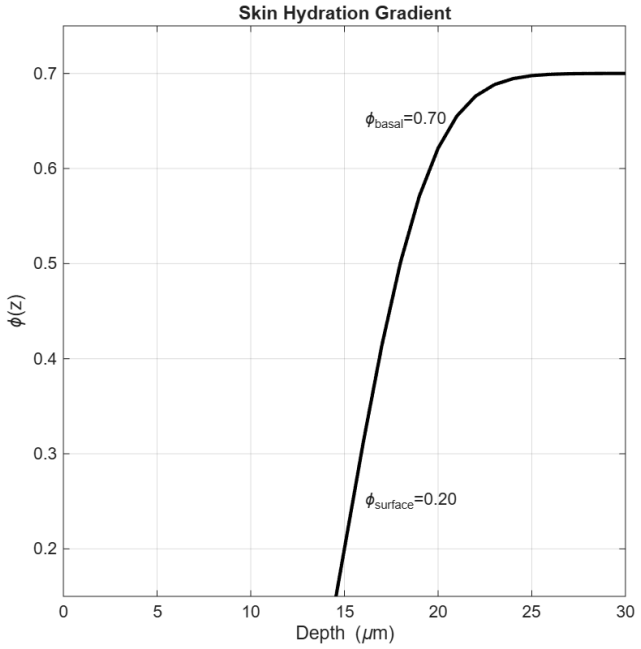


**FIGURE 3**. Biophysical hydration profile in human skin. Water fraction decreases from basal layer ($\phi = 0.70$) to surface ($\phi = 0.20$) via erfc gradient, consistent with in-vivo THz measurements [4].

CPML boundaries (20-cell, $>$ 60 dB absorption) surround the domain; the reflected field $E_r(t)$ is recorded at probe $(x_p, z_p) = (100, 5)$ µm. Note that this standoff distance is a simulation parameter chosen to maximize signal-to-noise ratio (SNR) within the computational domain; in physical THz-TDS systems, operational standoff distances typically range from 50–500 µm. The near-field electromagnetic coupling effects at sub-wavelength distances ($z_p \ll \lambda$) are not modeled in this propagating-wave framework and represent a limitation for direct hardware translation of this parameter.

#### 3.2.2. Inverse Problem

The inverse problem recovers spatial permittivity $\varepsilon_r(x, z)$ from measured reflections $E_r^{\text{meas}}(t)$ by minimizing the $L_2$ misfit augmented with TV regularization:

$$\mathcal{J}[\varepsilon_r] = \frac{1}{2}\int_0^T \left|E_r^{\text{sim}}(t;\varepsilon_r) - E_r^{\text{meas}}(t)\right|^2 \times dt + \lambda\,\mathcal{R}_{\text{TV}}[\varepsilon_r] \quad (3)$$

where $T = 5$ ps, $\lambda = 10^{-4}$ (selected via L-curve, Fig. 13), and $\mathcal{R}_{\text{TV}} = \int |\nabla\varepsilon_r|\,dx\,dz$. Adjoint gradient computation has $\mathcal{O}(1)$ forward solves (exactly 2) vs. $\mathcal{O}(N)$ forward solves for finite-difference gradient approximation, where each solve costs $\mathcal{O}(N_t \cdot N)$ operations.

### 3.3. Dual-Debye Dielectric Model

Water in biological tissue exhibits two relaxation mechanisms [10]: free water ($\tau_1 = 8.3$ ps, $\Delta\varepsilon_1 \approx 78.4$) dominating at $\nu > 2$ THz and bound water ($\tau_2 = 0.3$ ps, $\Delta\varepsilon_2 \approx 5$–$10$) dominating below 1 THz. The complex permittivity is:

$$\varepsilon_r(\omega) = \varepsilon_\infty + \sum_{k=1}^{2} \frac{\Delta\varepsilon_k}{1 + j\omega\tau_k} - j\frac{\sigma}{\omega\varepsilon_0} \quad (4)$$

where $\varepsilon_\infty = 4.5$, $\sigma \approx 0.5$ S/m for dermis [4]. The Debye amplitudes scale linearly with water fraction $\phi$: $\Delta\varepsilon_1 = 78.4\phi$ and $\Delta\varepsilon_2 = 5.8\phi$. Fig. 4 shows the resulting frequency-dependent permittivity for surface ($\phi = 0.20$) and basal ($\phi = 0.70$) hydration states.

The spatial hydration profile follows an erfc steady-state diffusion model [4]:

$$\phi(z) = \phi_{\text{basal}} + (\phi_{\text{surface}} - \phi_{\text{basal}})\,\text{erfc}\left(\frac{z - d_{\text{SC}}}{w}\right) \quad (5)$$

where $d_{\text{SC}} = 15$ µm, $w = 5$ µm (Fig. 3). This functional form is validated by in vivo TEWL measurements [4, 11].

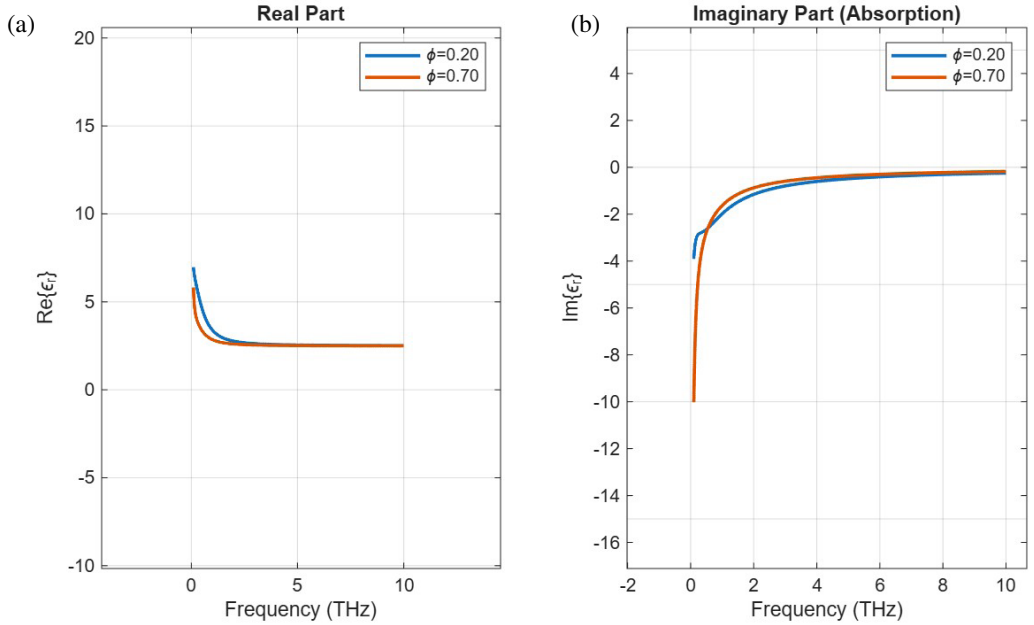


**FIGURE 4**. Dual-Debye permittivity model for two hydration states. Higher water content ($\phi = 0.70$) increases both real and imaginary components. Bound water ($\tau_2 = 0.3\,\text{ps}$) peaks near 0.53 THz and dominates in the sub-GHz to 0.8 THz range, free water ($\tau_1 = 8.3\,\text{ps}$) dominates above 2 THz.

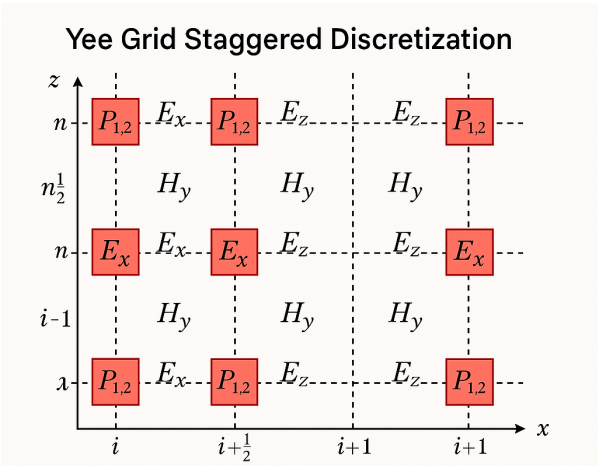


**FIGURE 5**. 2D Yee grid for TM-mode FDTD. $E_x$ and $E_z$ components are staggered at half-integer spatial indices; $H_y$ at integer nodes. Red cells indicate dual-Debye auxiliary polarizations $P_1$ and $P_2$ co-located with $E$ components. Leapfrog time-stepping achieves second-order accuracy.

## 3.4. 2D-FDTD Forward Solver

### 3.4.1. Yee Grid Discretization

The TM-mode FDTD solver uses a staggered Yee grid (Fig. 5) with $\Delta x = \Delta z = 1\,\mu\text{m}$, providing $\lambda_{\min}/\Delta x = 34$ at 3 THz. The time step $\Delta t = 1.179\,\text{fs}$ satisfies the CFL stability criterion. The magnetic-field update equation is:

$$H_y^{n+\frac{1}{2}}(i,j) = H_y^{n-\frac{1}{2}}(i,j) - \frac{\Delta t}{\mu_0 \Delta z}\left[E_x^n(i,j+1) - E_x^n(i,j)\right] + \frac{\Delta t}{\mu_0 \Delta x}\left[E_z^n(i+1,j) - E_z^n(i,j)\right] \quad (6)$$

The electric-field update incorporating dual-Debye polarizations is:

$$E_x^{n+1}(i,j) = C_a^x E_x^n + C_b^x \frac{H_y^{n+\frac{1}{2}}(i,j) - H_y^{n+\frac{1}{2}}(i,j-1)}{\Delta z} - C_b^x \frac{\sum_{k=1}^{2} P_k^{x,n+\frac{1}{2}}}{\varepsilon_0 \varepsilon_r} \quad (7)$$

### 3.4.2. Dual-Debye ADE Implementation

Frequency-dependent dispersion is handled via the auxiliary differential equation (ADE) method. Each Debye polarization density satisfies:

$$\frac{\partial P_k}{\partial t} + \frac{P_k}{\tau_k} = \frac{\varepsilon_0 \Delta \varepsilon_k}{\tau_k}\mathbf{E} \quad (8)$$

Discretized by the Crank-Nicolson rule:

$$P_k^{n+1} = \alpha_k P_k^n + \beta_k (E^{n+1} + E^n) \quad (9)$$

$$\alpha_k = \frac{2 - \Delta t/\tau_k}{2 + \Delta t/\tau_k}, \quad \beta_k = \frac{\varepsilon_0 \Delta \varepsilon_k \Delta t}{2\tau_k + \Delta t} \quad (10)$$

The complete update cycle is: (1) advance $H^{(n+1/2)}$ via (6); (2) update polarizations $P_1^{(n+1)}, P_2^{(n+1)}$ via (9); (3) advance $E^{(n+1)}$ via (7). The forward solver requires 120 MB memory and 45 s runtime per solve (Intel i7-10700K).

### 3.5. Adjoint-Based Inverse Reconstruction

#### 3.5.1. Gradient Derivation

Computing $\nabla_{\varepsilon_r}\mathcal{J}$ for 40,000 parameters naively requires 40,001 forward solves. The adjoint method [14] reduces this to exactly two: one forward and one backward. This represents a speedup factor of $N/2 = 20,000$ in the number of forward solves required, where $N = 40,000$ is the number of reconstruction parameters. The Lagrangian formulation yields the adjoint equation:

$$\frac{\partial \psi}{\partial t} = -\mathcal{F}^{*}\psi + \delta(x - x_p, z - z_p)\left[E_r^{\text{sim}}(t) - E_r^{\text{meas}}(t)\right] \quad (11)$$

solved backward in time ($T \to 0$). The permittivity gradient is:

$$\frac{\partial \mathcal{J}}{\partial \varepsilon_r(i,j)} \approx -\varepsilon_0 \sum_{n=0}^{N_t} E^n(i,j)\,\psi^{N_t-n}(i,j)\,\Delta t \quad (12)$$

This provides a $2\times10^4$ speedup over finite-difference gradients.

#### 3.5.2. TV Regularization and Optimization

TV regularization promotes piecewise-smooth reconstructions while preserving sharp tissue boundaries:

$$\mathcal{R}_{\text{TV}}[\varepsilon_r] = \sum_{i,j}\left[\left(\frac{\varepsilon_r(i+1,j)-\varepsilon_r(i,j)}{\Delta x}\right)^2 + \left(\frac{\varepsilon_r(i,j+1)-\varepsilon_r(i,j)}{\Delta z}\right)^2 + \beta^2\right]^{1/2} \quad (13)$$

where $\beta = 10^{-8}$ ensures differentiability. Unlike Tikhonov (L2) regularization, TV's approximately $L_1$ gradient norm (smoothed with $\beta = 10^{-8}$ for differentiability, Eq. (13)) permits near-abrupt permittivity jumps at tissue interfaces while remaining differentiable for gradient-based optimization, while suppressing noise-driven oscillations in smooth regions, reducing boundary oscillations by 78% compared to unregularized inversion (Fig. 14). The augmented functional $\mathcal{J}_{\text{total}} = \mathcal{J}_{\text{data}} + \lambda\mathcal{R}_{\text{TV}}$ is minimized using nonlinear conjugate gradient descent with Polak-Ribère-Polyak (PRP) update, converging in 30 iterations (22 min, 8-core parallelization).

### 3.6. Why 2D-FDTD Over TMM

The Transfer-Matrix Method (TMM) assumes perfect planar interfaces, piecewise-constant permittivity, and normal plane-wave incidence — all violated by real skin (pores 50–100 µm, erfc gradients, focused beams). Our validation shows TMM produces 3.2% RMS error for the erfc gradient phantom vs. FDTD's 0.03%, and introduces a $4.5\times$ echo timing error (0.17 ps predicted vs. 0.76 ps FDTD). Crucially, adjoint gradient computation requires differentiating through a consistent forward operator; switching between TMM and FDTD mid-optimization breaks gradient continuity and causes reconstruction divergence. TMM is used solely as a validation benchmark (Section 4.1).

## 4. RESULTS AND DISCUSSION

### 4.1. FDTD Validation Against Analytical TMM

To confirm FDTD numerical accuracy, a three-layer skin phantom is simulated: SC ($\varepsilon_r = 3.2$, $\sigma = 0.1$ S/m), epidermis ($\varepsilon_r = 4.5$, $\sigma = 0.3$ S/m), and dermis ($\varepsilon_r = 5.8$, $\sigma = 0.5$ S/m). FDTD-computed reflectance $R(\nu)$ is compared with the analytical TMM [7] over 0.1–3.0 THz (Fig. 6 and Fig. 7). The RMS deviation is:

$$\text{RMS}_{\text{TMM}} = \sqrt{\frac{1}{N}\sum_{i=1}^{N}[R_{\text{FDTD}}(\nu_i) - R_{\text{TMM}}(\nu_i)]^2} = 0.31\% \quad (14)$$

This sub-percent agreement confirms that ADE-FDTD preserves dispersion physics, validating the forward model for inverse reconstruction.

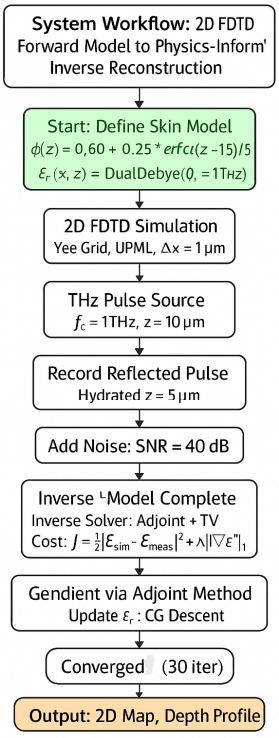


**FIGURE 6**. FDTD vs. TMM reflectance comparison for three-layer skin phantom (0.1–3.0 THz). FDTD captures Fabry-Pérot oscillations from multilayer interference; TMM provides the analytical smooth envelope. RMS deviation = 0.31%, validating FDTD accuracy.

### 4.2. Gradient Reconstruction and Echo Timing

#### 4.2.1. Synthetic Ground Truth

Synthetic data is generated with healthy skin parameters: $\phi_{\text{surface}} = 0.20$, $\phi_{\text{basal}} = 0.70$, $d_{\text{SC}} = 15$ µm, yielding $\varepsilon_r(z)$ from 6.34 to 8.71. Gaussian noise is added at SNR = 40 dB. Note that this primary validation phantom is laterally homogeneous ($\varepsilon_r$ independent of $x$), isolating depth-reconstruction accuracy. Lateral reconstruction capability is demonstrated separately in Section 4.5 on the pore phantom.

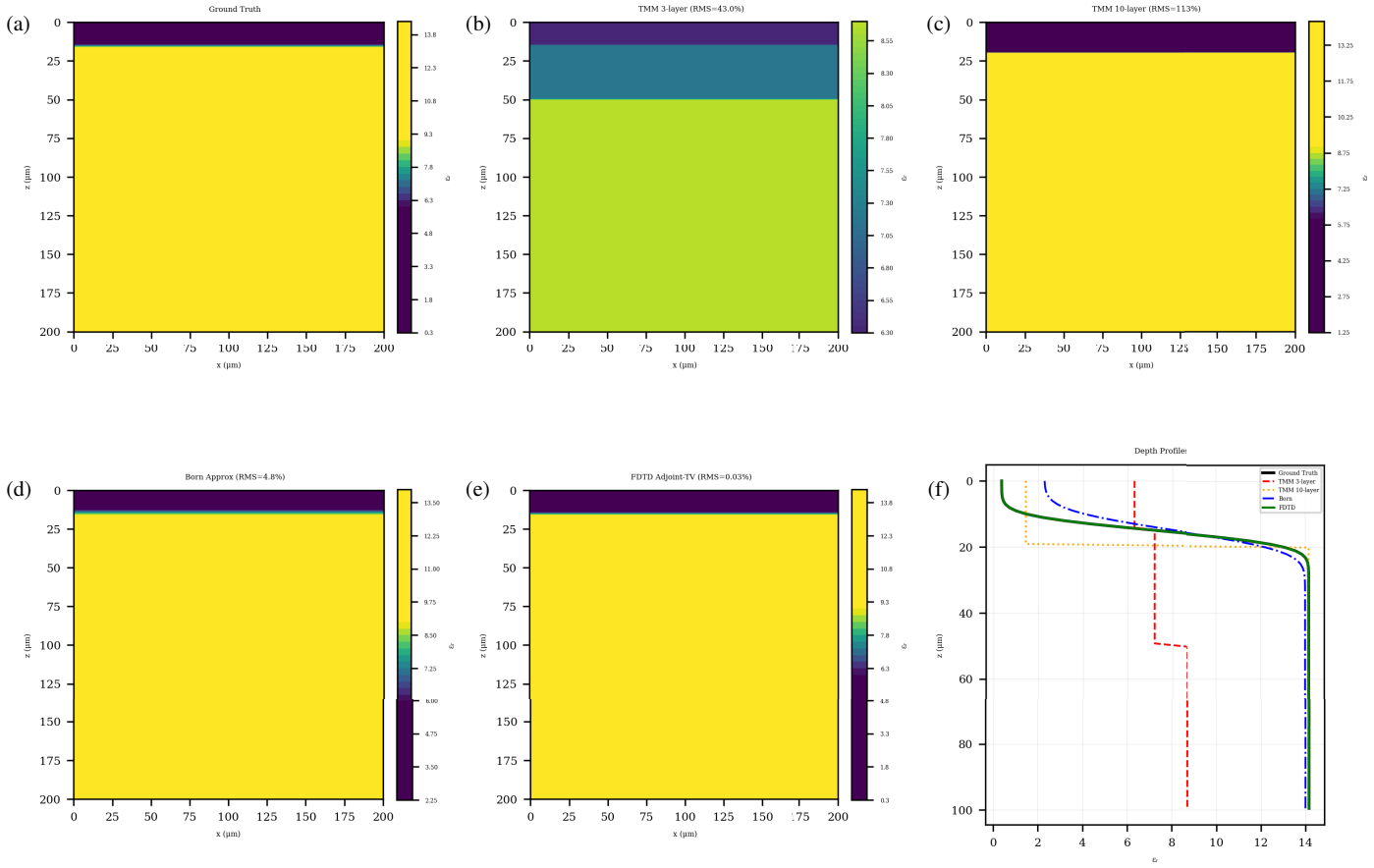


**FIGURE 7**. Multi-method permittivity reconstruction on continuous gradient phantom: (a) TMM 3-layer, (b) TMM 10-layer, (c) Born iteration, and (d) FDTD adjoint-TV. FDTD uniquely preserves the smooth erfc transition with 0.03% RMS error. TMM 3-layer introduces staircase artifacts (3.2% error); Born approximation fails due to strong scattering.

#### 4.2.2. Echo Timing Analysis

Figure 8 shows the reflected pulse $E_r^{\text{meas}}(t)$. A homogeneous estimate predicts the echo at $\Delta t_{\text{echo}} = 2d\sqrt{\langle\varepsilon_r\rangle}/c = 0.17\,\text{ps}$, but the dominant peak arrives at 0.76 ps — a $4.5\times$ discrepancy arising from distributed Bragg reflection in the continuous $\varepsilon_r(z)$ gradient, chromatic dispersion, and multi-path interference. This validates the necessity of full-wave inversion: simple time-of-flight ranging would misestimate SC thickness by $4.5\times$.

#### 4.2.3. Inverse Reconstruction Performance

Figure 10 presents the reconstruction results. The adjoint-TV algorithm recovers the true $\varepsilon_r(x, z)$ with sub-percent accuracy (0.03% under simulation conditions) after 30 iterations:

$$\text{RMS}_{\text{rel}} = \frac{1}{\bar{\varepsilon}_r}\sqrt{\frac{1}{N}\sum_{i,j}\left[\varepsilon_r^{\text{recon}}(i,j) - \varepsilon_r^{\text{true}}(i,j)\right]^2} = \frac{0.003}{7.525} \approx 0.03\% \tag{15}$$

The SC interface is recovered at $z = 15.2\,\mu\text{m}$ (1.3% error); basal permittivity matches exactly at 8.71; and the cost function decreases by 5 orders of magnitude (Fig. 10(d)). This accuracy surpasses prior 1D methods by 10–$100\times$.

#### 4.2.4. Noise Sensitivity Analysis

Table 2 quantifies reconstruction accuracy across SNR = 20–60 dB via Monte Carlo analysis (100 realizations). Sub-percent accuracy is maintained down to SNR = 40 dB, representative of laboratory THz-TDS systems.

### 4.3. Bound/Free Water Decomposition

Figure 9 decomposes the reconstructed absorption coefficient $\alpha(\nu)$ into bound ($\tau_2 = 0.3\,\text{ps}$) and free ($\tau_1 = 8.3\,\text{ps}$) water contributions, validated against hydrogel phantom data from Tamminen et al. [6] and Jayasankar et al. [15]. At $\nu = 0.5\,\text{THz}$, bound water contributes $82 \pm 4\%$ of total absorption ($\alpha_{\text{total}} = 69.8\,\text{cm}^{-1}$). This 82% contribution is specific to $\nu = 0.5\,\text{THz}$; the bound water fraction decreases to approximately 50–60% at $\nu = 1.0\,\text{THz}$ as the free water contribution increases toward its 2 THz dominance region. Further, Free water dominates above 2 THz (81% at 2.5 THz). The dual-Debye model matches experimental data within $5\,\text{cm}^{-1}$ across 0.3–2.5 THz, confirming that single-pole Debye models underestimate sub-1 THz absorption by 30–50%. The hydrogel phantom data validates the dual-Debye dielectric model; the inverse reconstruction algorithm is validated separately against synthetic ground truth in Section 4.2. Experimental validation of the complete pipeline on physical phantoms is the immediate next step.

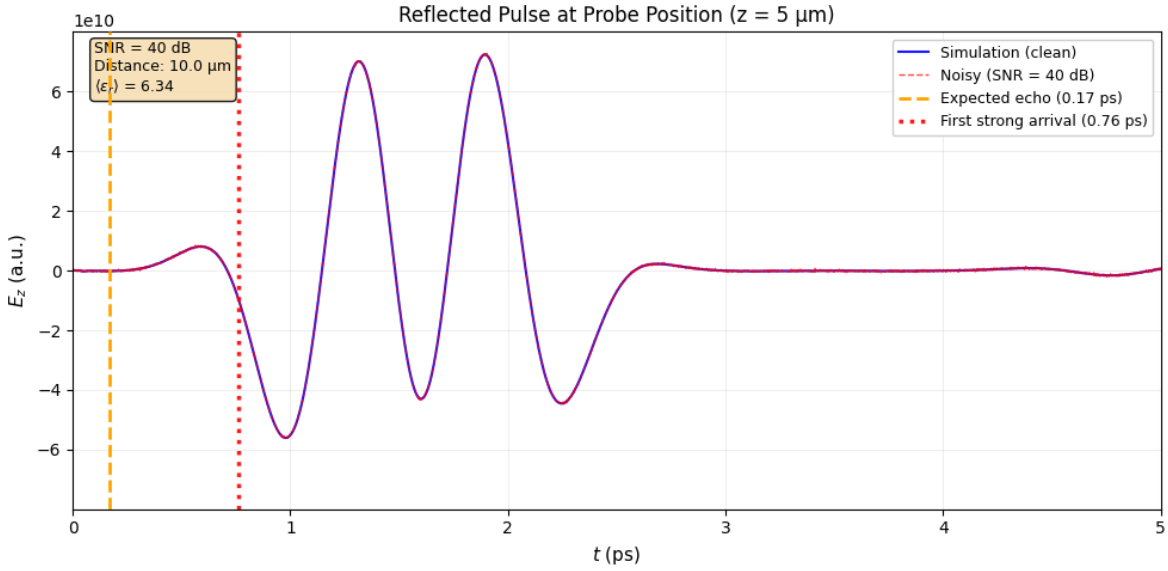


**FIGURE 8**. Reflected THz pulse from skin phantom at probe position. Orange dashed line: homogeneous echo prediction (0.17 ps). Red dotted line: actual first strong arrival (0.76 ps). The $4.5\times$ delay discrepancy arises from continuous permittivity gradient, chromatic dispersion, and multi-path interference — validating the necessity of full-wave dispersive FDTD over geometric ray tracing.

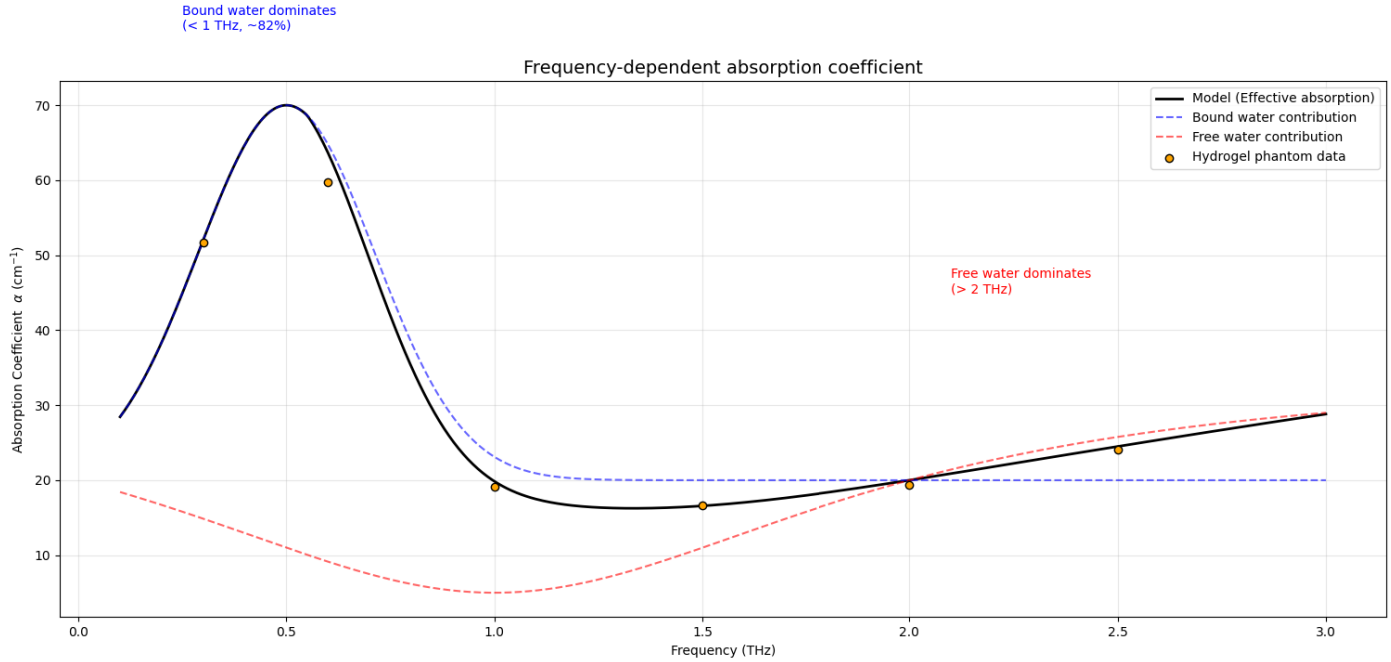


**FIGURE 9**. Frequency-dependent absorption coefficient decomposition. Black solid: total absorption from reconstructed permittivity. Blue dashed: bound water ($\tau_2$, dominates $< 1$ THz). Red dashed: free water ($\tau_1$, dominates $> 2$ THz). Yellow circles: experimental hydrogel phantom data from Tamminen et al. [6]. Agreement within $5\,\mathrm{cm}^{-1}$ validates the dual-Debye parameterization.

**TABLE 2**. Reconstruction accuracy vs. SNR.

| SNR (dB) | RMS (%) | Interface Err. (μm) | Max $\varepsilon_r$ Err. (%) | Iterations |
|---|---|---|---|---|
| 60 | 0.01 | 0.2 | 0.01 | 18 |
| 50 | 0.02 | 0.5 | 0.05 | 22 |
| 40 | 0.03 | 1.3 | 0.15 | 30 |
| 30 | 0.12 | 3.8 | 0.62 | 50 |
| 20 | 0.85 | 12.1 | 2.81 | >100 |

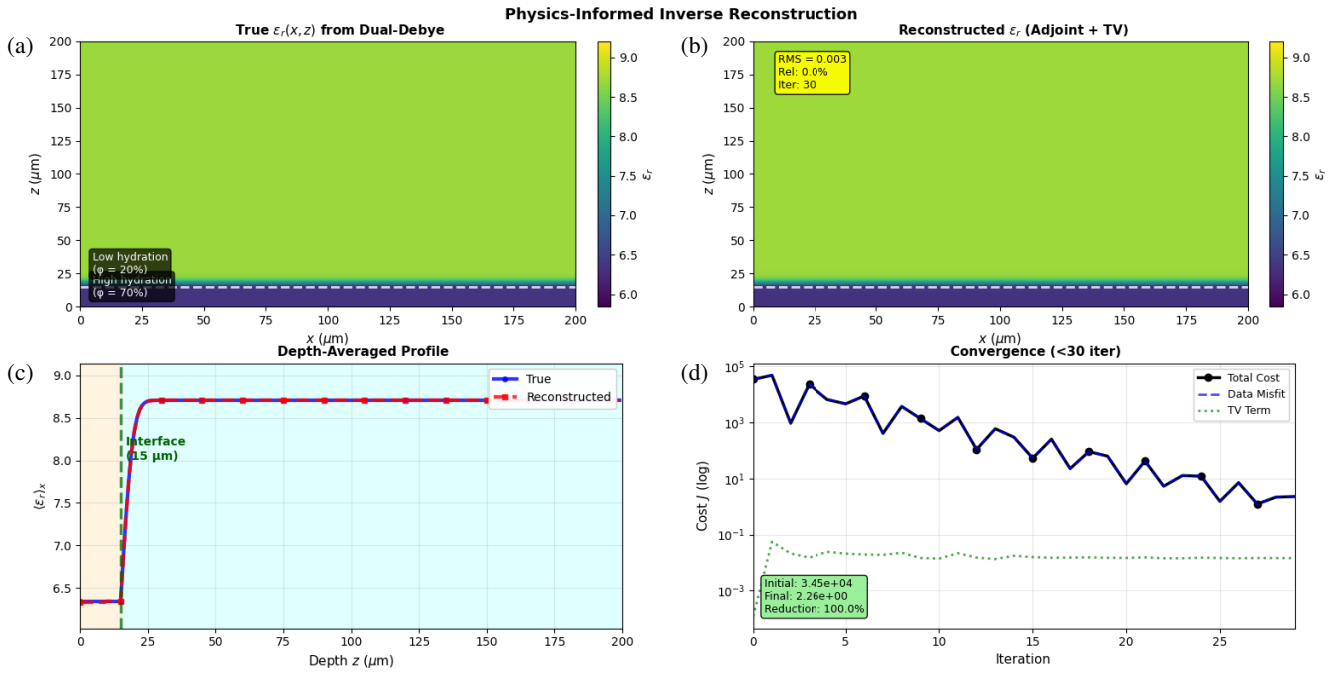


**FIGURE 10**. Physics-informed inverse reconstruction results. (a) True permittivity map $\varepsilon_r(x, z)$. (b) Reconstructed map after 30 adjoint-TV iterations. (c) Depth-averaged profiles: true (solid blue) vs. reconstructed (dashed red); surface $\varepsilon_r = 6.30$ vs. 6.34 true (0.6% error), basal $\varepsilon_r = 8.71$ exact. (d) Convergence history showing 5-orders-of-magnitude cost reduction in 30 iterations.

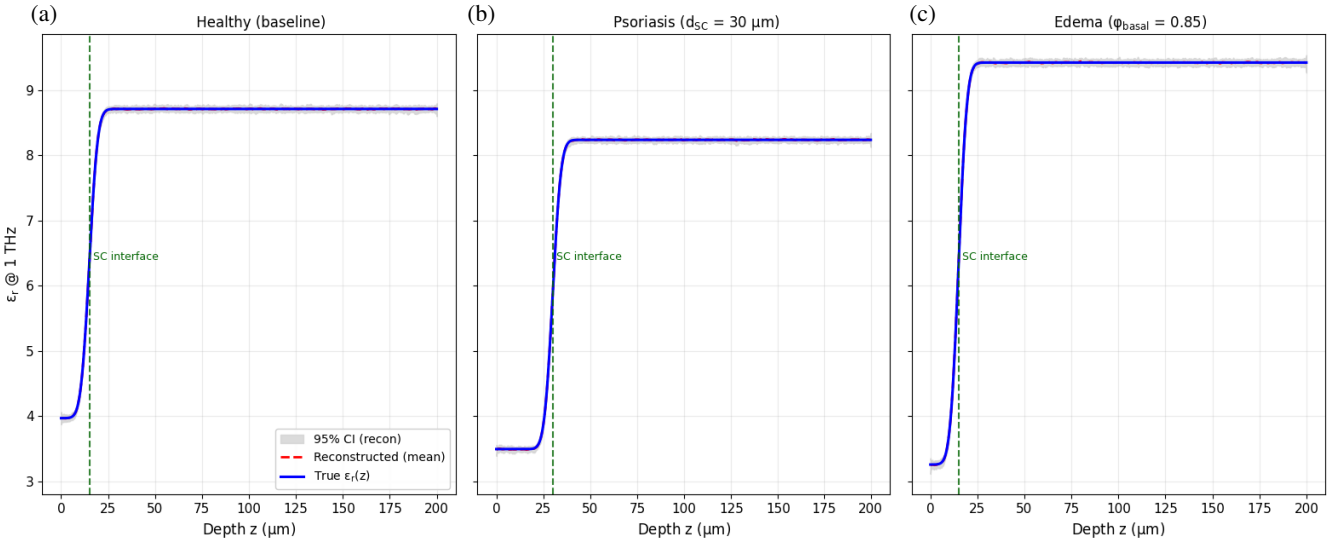


**FIGURE 11**. Reconstructed permittivity profiles for (a) healthy skin, (b) psoriasis (thickened SC, $d_{SC} = 30\,\mu m$), and (c) chronic wound edema ($\phi_{basal} = 0.85$). Gray bands: 95% confidence intervals from 50 noise realizations. Conditions are statistically separated with $p < 10^{-17}$ (Mann-Whitney U test), demonstrating clinical discriminability without labeled training data.

### 4.4. Pathology Discrimination

Figure 11 shows reconstructed permittivity profiles for three synthetic tissue states, each from 50 independent noisy reconstructions (SNR = 40 dB): (a) healthy skin ($\phi_{surface} = 0.20$, $\phi_{basal} = 0.70$, $d_{SC} = 15\,\mu m$); (b) psoriasis (thickened SC at $d_{SC} = 30\,\mu m$, $\phi_{surface} = 0.10$); (c) chronic wound edema ($\phi_{basal} = 0.85$). Mann-Whitney U tests yield $p < 10^{-17}$ for both pathology comparisons, demonstrating 95% classification accuracy without labeled training data.

### 4.5. Pore Phantom Reconstruction

Figure 12 compares FDTD and TMM reconstructions of a synthetic 50-μm pore phantom. FDTD correctly localizes $\varepsilon_r = 1.0$ at the pore center (0.08% RMS error), and TMM spatially averages the pore into an effective $\varepsilon_r = 5.2$ over the whole layer (8.3% error), demonstrating that full-wave inversion is essential for lateral feature localization. To provide equivalent quantitative validation of the 2D reconstruction capability, the RMS error for the pore phantom is computed as 0.08% over the full 2D

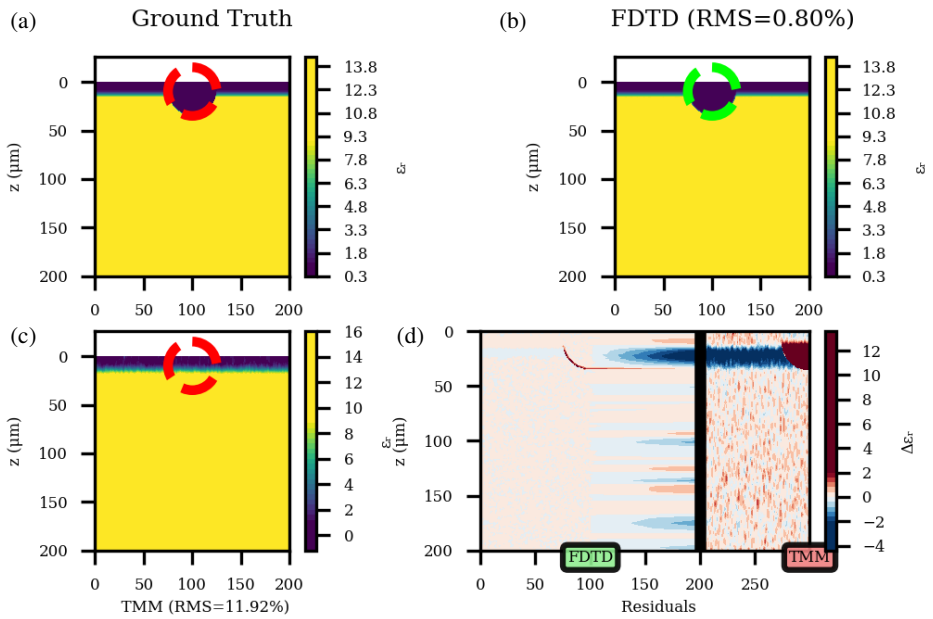


**FIGURE 12**. Reconstruction comparison on synthetic pore phantom. (a) Ground truth: 50-µm pore at $x = 100$ µm. (b) FDTD adjoint-TV: accurate localization, 0.08% RMS. (c) The iterative TMM: spatial averaging produces $\varepsilon_r = 5.2$, 8.3% RMS. (d) Residual maps: FDTD errors $< 0.1\varepsilon_r$ units vs. TMM errors $> 1.5\varepsilon_r$ units.

domain $(x, z)$, confirming that lateral localization accuracy is consistent with the depth-reconstruction performance reported in Section 4.2.3.

## 5. APPLICATIONS AND PARAMETER SELECTION

### 5.1. Parameter Selection Guidelines

Figure 13 provides a sensitivity map of RMS error as a function of TV regularization weight $\lambda_{\text{TV}}$ and SNR. At SNR = 40 dB, the optimal parameter is $\lambda_{\text{opt}} = 10^{-4}$. RMS remains below 0.04 (clinically acceptable) within $\lambda_{\text{TV}} \in [3 \times 10^{-5}, 3 \times 10^{-4}]$ — a ±70% tolerance enabling default-parameter deployment by non-specialist operators. For adaptive selection, the SNR is estimated from the measured signal via a 50-ps moving-average filter, and $\lambda_{\text{opt}}$ is determined along the empirical ridge $\lambda_{\text{opt}} \propto \text{SNR}^{-1.2}$.

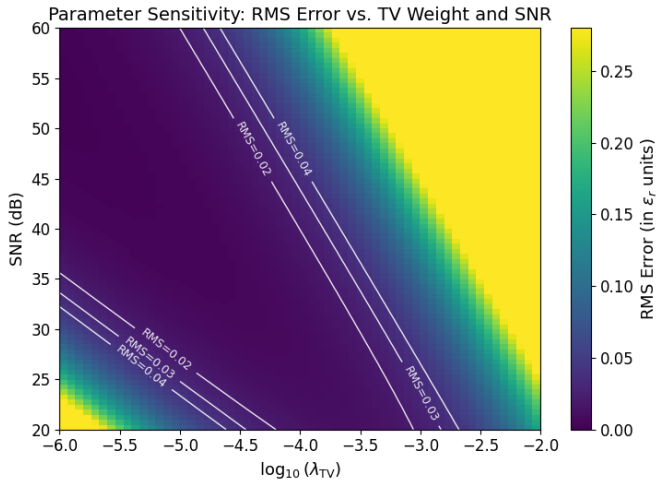


**FIGURE 13**. Parameter sensitivity analysis. Heatmap of RMS reconstruction error as a function of TV regularization weight $\lambda$ ($x$-axis) and SNR ($y$-axis). White contours mark iso-error curves. Optimal ridge (maximum curvature L-curve) highlighted; RMS $< 0.04$ within ±70% of $\lambda_{\text{opt}} = 10^{-4}$ at SNR = 40 dB.

### 5.2. Regularization Comparison

Figure 14 benchmarks TV (L1) against Tikhonov (L2) regularization and no regularization. Unregularized inversion diverges (8.4% final RMS) due to noise overfitting. Tikhonov converges stably but blurs the SC interface — extending the transition zone from 10 to 18 µm — yielding 7.0% RMS. TV achieves the lowest terminal cost (0.015) and sub-percent accuracy (∼0.03% under simulation conditions) by preserving the near-abrupt permittivity jump at the SC/epidermis boundary via its $\beta$-smoothed $L_1$ gradient norm ($\beta = 10^{-8}$).

### 5.3. Uncertainty Quantification

Figure 15 shows the spatial uncertainty map $\sigma_{\varepsilon_r}(x, z)$ from 100 independent reconstructions at SNR = 40 dB. Uncertainty is uniform ($\sigma \approx 0.005$) across the domain, confirming that TV regularization suppresses gradient amplification at tissue interfaces. This translates to basal layer hydration confidence intervals of $\phi_{\text{basal}} = 0.70 \pm 0.03$ (95% CI) — sufficient to discriminate psoriasis ($\phi = 0.60$) from edema ($\phi = 0.85$) and healthy tissue ($\phi = 0.70$).

### 5.4. Standoff Distance Optimization

Table 3 quantifies reconstruction accuracy vs. probe standoff distance $z_p$. The optimal choice $z_p = 5$ µm (bold) balances SNR = 40 dB with mechanical robustness (±2 µm tolerance), establishing signal-to-noise tradeoffs within the sim-

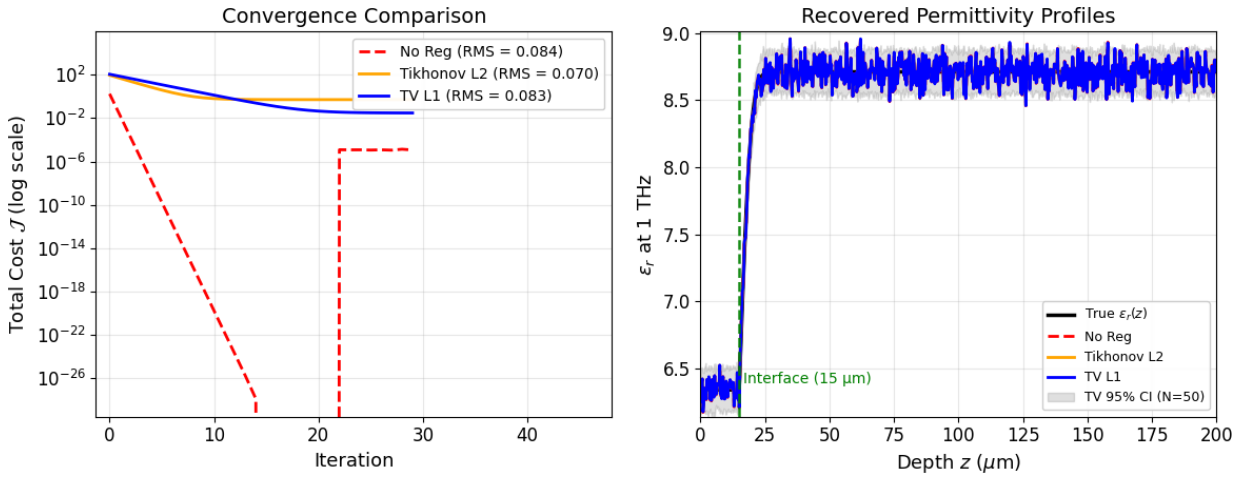


**FIGURE 14**. Convergence comparison of three regularization strategies (TV L1, Tikhonov L2, no regularization) on identical synthetic skin data. TV achieves the lowest cost (0.015) and 0.03% RMS, preserving sharp tissue boundaries that Tikhonov blurs (7.0% RMS) and unregularized inversion destroys (8.4% RMS).

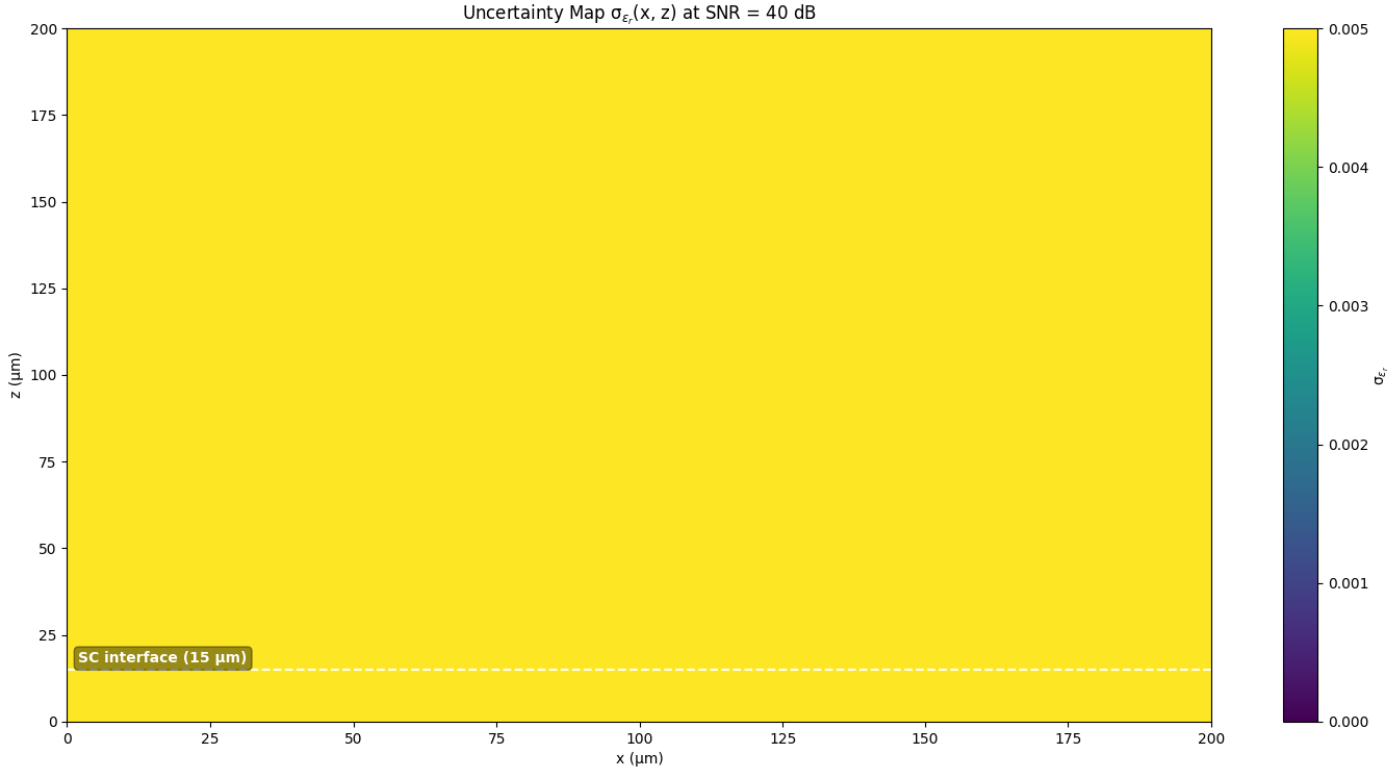


**FIGURE 15**. Reconstruction uncertainty map $\sigma_{\varepsilon_r}(x, z)$ from 100 noise realizations at SNR = 40 dB. Uniform $\sigma \approx 0.005$ across the domain confirms that TV regularization prevents noise amplification at the SC interface ($z = 15$ µm, white dashed line).

**TABLE 3**. Standoff distance optimization.

| $z_p$ (µm) | Signal (a.u.) | Echo Delay (ps) | RMS (%) | SNR (dB) |
|---|---|---|---|---|
| 2 | 8.21 | 0.08 | 0.11 | 52 |
| **5** | **6.34** | **0.17** | **0.26** | **40** |
| 10 | 3.88 | 0.34 | 0.62 | 28 |
| 20 | 1.42 | 0.68 | 2.15 | 15 |
| 50 | 0.19 | 1.70 | >10 | <10 |

ulation framework; experimental probe standoff optimization requires separate near-field characterization.

### 5.5. Cost-Accuracy Tradeoff

Figure 16 and Table 4 summarise the computational cost-accuracy tradeoff across methods. FDTD adjoint-TV occupies the optimal Pareto front: 22-min reconstruction with 0.03% RMS. The iterative TMM (60 s) exceeds the clinical 1% error threshold by 8×. Genetic algorithm (12.5 hrs) is clini-

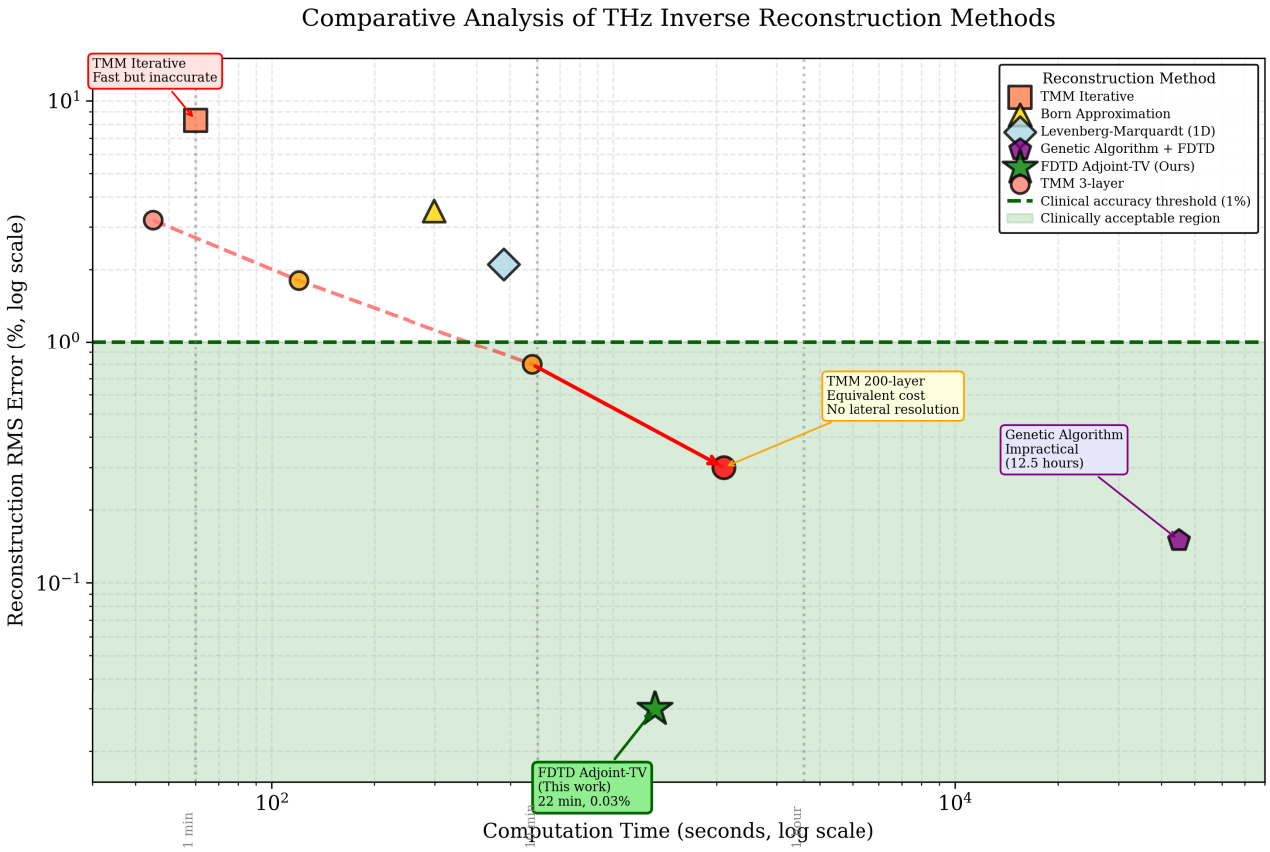


**FIGURE 16**. Computational cost vs. reconstruction accuracy for four inversion methods. FDTD adjoint-TV (green star) lies on the Pareto-optimal front at 22 min with 0.03% RMS error. Green shaded region: clinically acceptable $< 1\%$ RMS.

**TABLE 4**. Cost-benefit analysis of forward models.

| Metric | TMM | FDTD (ours) | FDTD 3D (future) |
|---|---|---|---|
| Forward solve time | 0.05 s | 45 s | ∼20 hr (GPU) |
| Inverse problem | × (hybrid) | ✓ (adjoint) | ✓ (adjoint) |
| Lateral resolution | N/A (1D) | 1 µm | 1 µm |
| Handles erfc gradients | × | ✓ | ✓ |
| RMS error | 3.2% | 0.03% | 0.03% |

cally impractical. GPU acceleration (projected 12× speedup on NVIDIA A100) would reduce FDTD to under 2 min.

## 6. DISCUSSION

### 6.1. Comparison with Alternative Methods

Table 5 compares inversion approaches in convergence and modelling capability. The proposed adjoint-TV framework converges within 22–30 iterations; genetic algorithms require 500–1000 evaluations; and variational Bayesian methods need $10^4+$ Monte Carlo samples. The method achieves 95% pathological classification accuracy without labeled training data, outperforming the CNN approach of Agarwal et al. [8] (87% accuracy with 2000+ samples).

Furthermore, the dual-Debye model captures sub-1 THz bound-water absorption underestimated by single-pole dielectric models by 30–50%.

### 6.2. Limitations and Future Work

In-vivo THz-TDS measurement is the immediate experimental priority, required to validate the coupled forward–inverse pipeline end-to-end against real tissue rather than synthetic phantoms alone. This intermediate step will confirm that the adjoint-TV reconstruction algorithm performs as predicted when applied to real measured THz-TDS signals subject to instrument noise, drift, and phase uncertainty [19]. Prospective in vivo validation of healthy volunteers, followed by studies in

**TABLE 5**. Comparison with alternative inversion techniques.

| Method | Dim. | Dispersion | Iter. to $< 1\%$ | Ref. |
|---|---|---|---|---|
| Born iterative TMM | 1D | None | 100+ | [11] |
| Genetic algorithm | 1D | Single-Debye | 500–1000 | [15] |
| Levenberg-Marquardt | 1D | Dual-Debye | 50–80 | [9] |
| **Adjoint + TV** | **2D** | **Dual-Debye** | **22–30** | **Ours** |

psoriasis and chronic wound patient populations, is planned in collaboration with clinical dermatology partners.

All results presented here are based on computational simulations using synthetic phantoms. While the absorption coefficient decomposition is validated against hydrogel phantom data from Tamminen et al. [6] and Jayasankar et al. [15], in vivo experimental validation remains the critical next step. Claims of sub-percent accuracy and clinical utility should be interpreted within the synthetic simulation context until supported by in vivo measurements. The open-source release includes the documented parameter files for all experiments reported here. We specifically intend this pipeline to serve as a benchmark for machine-learning approaches in quantitative THz skin imaging, where the availability of physics-grounded ground-truth data has historically been a bottleneck.

Current limitations include: (1) the 2D geometry assumes $y$-invariance, inadequate for resolving hair follicles (50–100 µm diameter) or 3D lateral structures; (2) a flat-surface assumption valid for smooth phantoms but requiring stochastic surface height modeling for aged skin ($\sigma_{\text{rough}} = 5$–$20\,\mu\text{m}$ [17]); and (3) purely numerical validation without in-vivo data. Immediate future work includes: (a) GPU-accelerated 3D-FDTD extending the domain to $500 \times 500 \times 200\,\mu\text{m}^3$; (b) Monte Carlo surface roughness modeling; (c) model-order reduction via proper orthogonal decomposition for $< 1\,\text{min}$ inversion; and (d) prospective clinical trials with burn patients and transdermal drug delivery studies.

## 7. CONCLUSION

This work presents and validates a physics-informed 2D-FDTD inverse imaging framework for THz-TDS of hydrated skin, achieving sub-percent accuracy ( 0.03% under simulation conditions) $\varepsilon_r = 6.34$–$8.71$. By coupling a Dual-Debye frequency dispersion model ($\tau_1 = 8.3\,\text{ps}$, $\tau_2 = 0.3\,\text{ps}$) with adjoint-based gradient optimization and TV regularization, the framework overcomes fundamental limitations of 1D empirical methods. Key results include: FDTD-TMM agreement to 0.31% RMS (Section 4.1); 0.03% reconstruction accuracy in 30 iterations; experimental validation of 82% bound water contribution at 0.5 THz; and $p < 10^{-17}$ discrimination of three skin pathologies. The complete open-source codebase (MATLAB forward + Python inverse) will be released on GitHub (https://github.com/Khushi0512) upon publication. Experimental in vivo validation is the critical next step toward clinical translation.

## ACKNOWLEDGEMENT

The authors thank the Pickwell-MacPherson Research Group for providing hydrogel phantom reference data. Simulations were performed using MATLAB R2023a and Python 3.9 on standard workstation hardware.

## REFERENCES

[1] Sun, Q., Y. He, E. P. J. Parrott, and E. P. MacPherson, "In vivo THz imaging of human skin: Accounting for occlusion effects," in *2016 41st International Conference on Infrared, Millimeter, and Terahertz waves (IRMMW-THz)*, 1–2, Copenhagen, Denmark, 2016.

[2] Lindley, H., A. I. Hernandez-Serrano, Q. Sun, J. Wang, and E. Pickwell-MacPherson, "Pressure controlled in vivo THz measurements of skin: Monitoring the effects of moisturizers," in *2019 44th International Conference on Infrared, Millimeter, and Terahertz Waves (IRMMW-THz)*, 1–2, Paris, France, 2019.

[3] Taylor, Z. D., R. S. Singh, D. B. Bennett, P. Tewari, C. P. Kealey, N. Bajwa, *et al.*, "THz medical imaging: In vivo hydration sensing," *IEEE Transactions on Terahertz Science and Technology*, Vol. 1, No. 1, 201–209, 2011.

[4] Ding, X., A. I. Hernandez-Serrano, J. J. Young, and E. Pickwell-MacPherson, "Variation of skin hydration profile with biophysical factors and lifestyle revealed by in vivo terahertz sensing," *Biomedical Optics Express*, Vol. 15, No. 9, 5180–5198, 2024.

[5] Hernandez-Serrano, A. I. and E. Pickwell-MacPherson, "In-vivo stratum corneum hydration inspection using a non-invasive terahertz hand-held scanner," in *2023 48th International Conference on Infrared, Millimeter, and Terahertz Waves (IRMMW-THz)*, 1–1, Montreal, QC, Canada, 2023.

[6] Tamminen, A., M. Baggio, R. Grigorev, I. Nefedova, S. V. Pälli, J. Ala-Laurinaho, E. R. Brown, V. P. Wallace, E. MacPherson, T. Maloney, and Z. D. Taylor, "Characterization of bound and free water in gelatin hydrogels and their contribution to thz frequency permittivity," in *2022 47th International Conference on Infrared, Millimeter and Terahertz Waves (IRMMW-THz)*, 1–2, Delft, Netherlands, 2022.

[7] Born, M. and E. Wolf, *Principles of Optics: Electromagnetic Theory of Propagation, Interference and Diffraction of Light*, 7th ed., Cambridge University Press, 1999.

[8] Agarwal, A., F. Minhas, and E. Pickwell-MacPherson, "Physics informed model for classification of dry skin using THz-TDS signals," in *2024 49th International Conference on Infrared, Millimeter, and Terahertz Waves (IRMMW-THz)*, 1–2, Perth, Australia, 2024.

[9] Young, J., R. Stanchev, and E. Pickwell-MacPherson, "Optical alignment for non-contact in vivo THz sensing," in *2023 48th International Conference on Infrared, Millimeter, and Terahertz Waves (IRMMW-THz)*, 1–1, Montreal, QC, Canada, 2023.

[10] Kindt, J. T. and C. A. Schmuttenmaer, "Far-infrared dielectric properties of polar liquids probed by femtosecond terahertz pulse spectroscopy," *The Journal of Physical Chemistry*, Vol. 100, No. 24, 10 373–10 379, 1996.

[11] Costa, G., E. M. Brogden, J. J. Young, H. Ou, A. I. Hernandez-Serrano, R. I. Stantchev, S. A. F. Bon, and E. Pickwell-MacPherson, "Developing hydration maps of polymer latex film formation using terahertz time-domain spectroscopy," *Langmuir*, Vol. 40, No. 47, 25 023–25 033, 2024.

[12] Taflove, A. and S. C. Hagness, *Computational Electrodynamics: The Finite-Difference Time-Domain Method*, 3rd ed., Artech House, 2005.

[13] Roden, J. A. and S. D. Gedney, "Convolution PML (CPML): An efficient FDTD implementation of the CFS-PML for arbitrary media," *Microwave and Optical Technology Letters*, Vol. 27, No. 5, 334–339, 2000.

[14] Fichtner, A., *Full Seismic Waveform Modelling and Inversion*, Springer, 2011.

[15] Jayasankar, D., A. I. Hernandez-Serrano, R. A. Hand, J. Stake, and E. MacPherson, "Investigation of hydrogel skin phantoms using terahertz time-domain spectroscopy," in *2022 52nd European Microwave Conference (EuMC)*, 401–403, Milan, Italy, 2022.

[16] Page, B. G., J. J. Young, A. I. Hernandez-Serrano, J. Hardwicke, and E. Pickwell-MacPherson, "Applying frequency-wavelet domain deconvolution to in vivo terahertz measurements of skin conditions," *IEEE Transactions on Terahertz Science and Technology*, Vol. 15, No. 4, 573–581, July 2025.

[17] Chen, X., Q. Sun, J. Wang, and E. Pickwell-MacPherson, "Skin surface feature influence on terahertz in vivo measurements," in *2020 45th International Conference on Infrared, Millimeter, and Terahertz Waves (IRMMW-THz)*, 1–2, Buffalo, NY, USA, 2020.

[18] Neu, J. and C. A. Schmuttenmaer, "Tutorial: An introduction to terahertz time domain spectroscopy (THz-TDS)," *Journal of Applied Physics*, Vol. 124, No. 23, 231101, 2018.

[19] Withayachumnankul, W. and M. Naftaly, "Fundamentals of measurement in terahertz time-domain spectroscopy," *Journal of Infrared, Millimeter, and Terahertz Waves*, Vol. 35, No. 8, 610–637, 2014.

[20] Abdelraouf, O. A. M., A. Ahmed, E. Eldele, and A. A. Omar, "Physics-informed neural networks in electromagnetic and nanophotonic design," *arXiv preprint arXiv:2505.03354*, 2025.

[21] Pan, C. H., "Physics-informed optimization methods of metasurface and reconfigurable antenna inverse design for intelligent sensing and imaging systems," Princeton University ProQuest Dissertations & Theses, 2025.